Monte Carlo modeling of an integrating sphere reflectometer

Alexander V. Prokhorov, Sergey N. Mekhontsev, and Leonard M. Hanssen

The Monte Carlo method has been applied to numerical modeling of an integrating sphere designed for hemispherical-directional reflectance factor measurements. It is shown that a conventional algorithm of backward ray tracing used for estimation of characteristics of the radiation field at a given point has slow convergence for small source-to-sphere-diameter ratios. A newly developed algorithm that substantially improves the convergence by calculation of direct source-induced irradiation for every point of diffuse reflection of rays traced is described. The method developed is applied to an integrating sphere reflectometer for the visible and infrared spectral ranges. Parametric studies of hemispherical radiance distributions for radiation incident onto the sample center were performed. The deviations of measured sample reflectance from the actual reflectance as a result of various factors were computed. The accuracy of the results, adequacy of the reflectance model, and other important aspects of the algorithm implementation are discussed. © 2003 Optical Society of America

OCIS codes: 000.4430, 000.5490, 120.0120, 120.3150, 120.5700, 120.4570.

1. Introduction

The integrating sphere (IS)—a hollow sphere with diffusely scattering (i.e., close to Lambert's law), high-reflectance internal walls—is one of the simplest and most widely used devices for optical radiation measurements. Because of its ability to redistribute nonuniform incident irradiation uniformly over its internal surfaces through multiple reflections, the IS finds applications in reflectance, transmittance, and luminous flux measurements and is used as a uniform radiance source. For the design of measurement instrumentation that uses ISs as well as for determining measurement uncertainties it is necessary to evaluate, compute, and predict the most important characteristics of the spheres. Irrespective of an IS's designated purpose, its principal radiometric characteristics are the spatial distribution of spectral irradiance over the internal surface of the IS and the angular distributions of spectral radiance incident on a given point or reflected from it. The radiation flux falling onto a detector, which is the

end point of any computation of ISs, can be found by integration of these distributions over appropriate spatial, angular, and spectral variables. Approximate IS theory is based on the summation of an infinite series of irradiances for consecutive diffuse reflections[1–3] and is applicable only to calculation of the average irradiation of IS walls. The exact solution for an IS with perfectly diffuse internal surfaces can be obtained numerically from Fredholm's integral equations of second kind.[4–6] This method allows such effects as vignetting of radiation by internal baffles and angular and spatial nonuniformity of source radiance to be accounted for. The zonal method,[7,8] based on the equation of radiant energy balance for finite areas that form the IS, is the discrete analog of the integral equations method. The common drawback of the above-mentioned methods is that their use is limited to ISs that have Lambertian surfaces. The reflection properties of real materials and coatings always differ from the Lambertian ideal. This difference can become considerable in the infrared spectral range, where the specular component of reflection can be significant. Therefore the use of the Lambertian model of reflection may lead to unpredictable errors. To date, the ray-tracing-based Monte Carlo method is the only technique that accommodates the direct simulation of non-Lambertian surfaces. The foundation of this technique is the probabilistic treatment of radiation–matter interactions. This approach permits construction of a stochastic model of the system under

The authors are with the Optical Technology Division, National Institute of Standards and Technology, Gaithersburg, Maryland 20899-8442. L. M. Hanssen's e-mail address is leonard.hanssen@nist.gov.

consideration and an evaluation of its parameters with a large number of ray-tracing implementations. The number of realizations of a stochastic process determines the accuracy of the solutions. Therefore, in the past several decades, along with the explosive growth of computer performance, the Monte Carlo method has seen increasing application to the radiometric problems of optical radiation transfer including numerical modeling of ISs.[9–12]

2. Statement of the Problem

The integrating sphere reflectometer that is being modeled will be employed to measure diffuse reflectance. In particular, it will measure the spectral hemispherical-conical reflectance factor (or, after application of the reciprocity theorem, the spectral conical-hemispherical reflectance) over a given wavelength and temperature range. The measurements are performed by the method of comparison with a reference (diffuse reflectance standard). The hemispherical-conical geometry (we use the nomenclature and definitions of reflection characteristics proposed by Nicodemus *et al*. in Ref. 13) implies uniform distribution of incident radiation over a hemispherical solid angle and collection of reflected radiation within a conical solid angle. The actual distribution of incident radiance is always nonuniform, which can result in an appropriate systematic uncertainty.

The research reported here has two main objectives: (i) to develop an algorithm and computer code to facilitate calculation of the hemispherical distribution of radiance for radiation falling onto the sample center as well as of the ratio of radiant fluxes reflected by the sample and the reference and (ii) to perform a parametric study of the quantities mentioned above against angular distribution of source radiant intensity, spectral reflectance, and its specular component for the sample and IS walls. The relative uncertainty of computations must be less than 0.1%. The computation model and the original algorithm of the Monte Carlo method developed to achieve these goals are described in Section 3.

A schematic cross section of the reflectometer is depicted in Fig. 1, where the y axis is directed behind the image plane. The IS (1) is coated with a high-reflectance diffuser over most of its surface. In the upper part of the IS there is an elliptical opening (2), intended for radiation output to a detector. A radiation source (3), located in the lower part of the IS directly opposite opening 2, is circular and nearly Lambertian (e.g., opal glass with fiber coupling to a halogen lamp or laser). A flat circular sample (4), encased in an annular holder (5) and connected with an outside thermostat (6), is arranged symmetrically to the reference (7) (diffuse reflectance standard), together with its own holder (8) and thermostat (9).

Two baffles (10) and (11), symmetrically placed between the radiation source and the sample and the reference, respectively, are intended to prevent their direct irradiation by the source. A concave folding mirror (12) that has a relative aperture of 1:7 is used
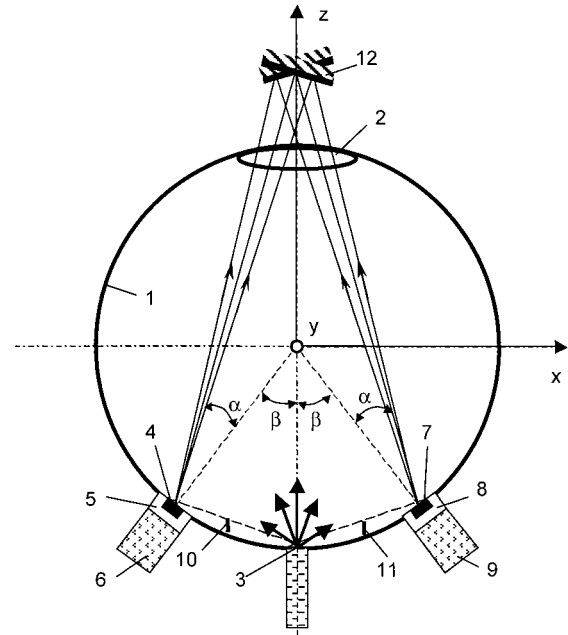

Fig. 1. Sectional view of the integrating sphere reflectometer: 1, integrating sphere; 2, elliptical opening; 3, radiation source; 4, sample; 5, sample holder; 6, sample thermostat; 7, reference; 8, reference holder; 9, reference thermostat; 10, 11, baffles; 12, folding mirror.

for alternate viewing of the radiation fluxes from the reference and the sample through the elliptical opening with a detector (e.g., a filter radiometer or spectrometer). The axes of the ray cones shown in Fig. 1 form equal angles α with the normals to sample and reference.

For an ideal reflectometer, sample spectral hemispherical-conical reflectance factor R_1 at temperature T_1 and for wavelength λ in conical solid angle Ω can be found from

$$\frac{R_1(\lambda,\ 2\pi \rightarrow \Omega,\ T_1)}{R_2(\lambda,\ 2\pi \rightarrow \Omega,\ T_2)} = \frac{V_1}{V_2}, \tag{1}$$

where V is the detector reading; throughout the paper the subscripts 1 and 2 denote sample and reference, respectively. For a small solid angle Ω and samples with a smooth bidirectional reflectance distribution function we can replace hemispherical-conical reflectance factor $R(\lambda,\ 2\pi \rightarrow \Omega,\ T)$ with hemispherical-directional reflectance factor $R(\lambda,\ 2\pi \rightarrow \omega,\ T)$, where direction ω coincides with the axis of conical solid angle Ω, in the notation $a \rightarrow b$, a and b represent illumination and collection geometries, respectively. According to the reciprocity theorem, hemispherical-directional reflectance factor $R(\lambda,\ 2\pi \rightarrow \omega,\ T)$ is equal to directional-hemispherical reflectance $\rho(\lambda,\ \omega \rightarrow 2\pi,\ T)$; then

$$\rho_1(\lambda,\ \omega \rightarrow 2\pi,\ T_1) = \rho_2(\lambda,\ \omega \rightarrow 2\pi,\ T_2) \frac{V_1(\lambda)}{V_2(\lambda)}. \tag{2}$$

Table 1. Numerical Values for IS Reflectometer Geometrical Parameters

Parameter	Symbol	Size	Unit
Sphere radius	r	127	mm
Opening largest half-axis	r_{0x}	30	mm
Opening shortest half-axis	r_{0y}	23	mm
Source radius	r_s	5	mm
Sample radius	r_1	9.5	mm
Sample holder radius	r_{h1}	17.5	mm
Reference radius	r_2	9.5	mm
Reference holder radius	r_{h2}	17.5	mm
Half-distance between baffles	x_b	15	mm
Baffle height	h_b	7	mm
Baffle half-length	y_b	17	mm
Central half-angle from sample to reference	β	16	deg
Viewing angle	α	8	deg

Fig. 2. Local spherical coordinate system.

Application of the reciprocity principle requires homogeneous and identical hemispherical irradiation of the sample and the reference.

3. Computational Model

The computational model of the IS under consideration (see Fig. 1) is formed by an internal spherical surface of radius r described by the equation

$$x^2 + y^2 + z^2 = r^2, \quad (3)$$

a flat radiation source of radius r_s lying in a plane parallel to the XY plane, two flat double-sided baffles, and symmetrically arranged holders of radii $r_{h1,2}$ with sample and reference of radii $r_{01,2}$. The axes of source, sample, and reference with their respective holders all lie in the XZ plane. The opening (exit port) is formed by the intersection of the spherical surface [Eq. (3)] with the upper part ($z > 0$) of the elliptic cylinder:

$$(x/r_x)^2 + (y/r_y)^2 = 1. \quad (4)$$

The boundary circumferences of source and holders are formed by sections of a sphere by appropriate planes. The baffles are plane segments parallel to the YZ plane and symmetrically distant on x_b from it. The bottom boundary of each baffle is formed by its intersection with the spherical surface. The maximum height of the baffle is h_b, and its length is $2y_b$.

For simplification we assume that conical fields of view of the foreoptics have vertices in sample and reference centers and that viewed areas are infinitesimal. All the geometrical parameters of the reflectometer are listed in Table 1.

To calculate the hemispherical distribution of incident radiance, we arranged the origin of the local spherical coordinate system in the sample center, as shown in Fig. 2.

In this paper we deal only with spectral (monochromatic) quantities (radiance, irradiance, radiant flux, reflectance, etc.), so the subscript λ is omitted. For elements of the integrating sphere, the uniform specular-diffuse model of reflection has been used.
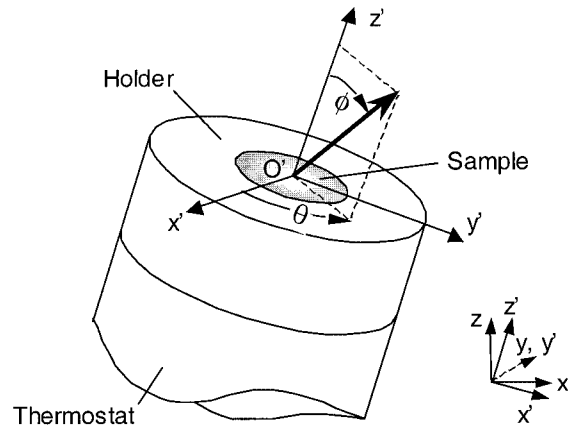
According to this model, the directional-hemispherical reflectance is a sum of perfectly diffuse (Lambertian) and specular components, and neither component depends on incident angle. Following the convention of Ref. 9, we describe each surface by the value of specularity S:

$$S = \rho_s/(\rho_s + \rho_d) = \rho_s/\rho, \quad (5)$$

where ρ_s and ρ_d are the specular and the diffuse components of reflectance, respectively, and ρ is their sum.

We assume that the radiation source has uniform spatial exitance: Each point of the source is Phong's luminaire[14] and emits with radiant intensity:

$$I(\theta) = \frac{\nu + 1}{2\pi} I(0)\cos^\nu \theta, \quad (6)$$

where θ is angle between the normal to the surface and the direction of observation (see Fig. 3). Because of the existence of a normalization factor, the source will have the same radiant flux for any value of ν.

We also assume that the reflective surfaces of the reference and the source are Lambertian and that the internal surface of the IS has the same specularity as the baffles. We allow the surface of the radiation source to have a nonzero reflectance. The values of reflectance for all surfaces of the IS reflectometer are listed in Table 2. The data for Variants 1 and 2 correspond to measurements in the infrared spectral range with the IS coated with plasma-sprayed gold; those for Variants 3 and 4 contain the reflectances for a visual spectral range and an IS made from Spectralon or an analogous material.

Finally, we assume geometrical (ray) optics and do not consider diffraction effects. We assume that either the radiation source emits unpolarized radiation or the radiation is effectively depolarized after multiple reflections inside the IS.
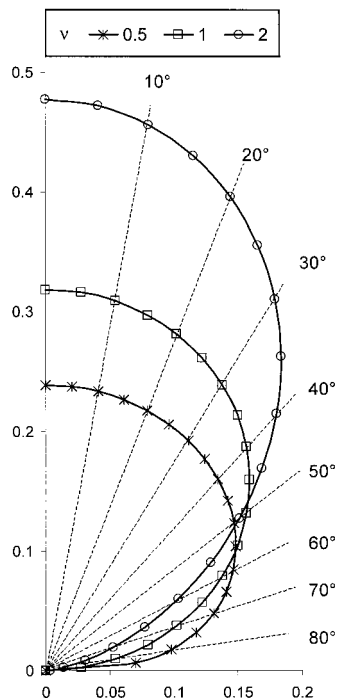
Fig. 3. Angular distributions of radiation source radiant intensity for $\nu = 0.5, 1, 2$.

4. Brute Force Monte Carlo Algorithm

In forward ray tracing, one traces a ray from the radiation source until it escapes through the exit port after several reflections inside the IS. If the directions of reflected rays are distributed randomly in the hemispherical solid angle, the geometrical probability of exact coincidence of a random direction with a given direction is equal to zero. This is why, if the radiation source is not itself a point, we use backward ray tracing (path tracing in computer graphics[15]). For backward ray tracing, in accordance with the reciprocity principle the ray starts to move in a given direction from the point under consideration and performs random walks inside the IS until it escapes through the exit port. The type of reflection—diffuse or specular—is chosen randomly according to the specularity. If a pseudorandom number η_s produced by the program's pseudorandom-number generator is less than the value of specularity S, the reflection is considered to be specular; otherwise it is

Table 2. Reflectances of IS Reflectometer Components

Component	Reflectance for Variant Number			
	1	2	3	4
Sphere internal surface	0.900	0.950	0.970	0.990
Baffles	0.900	0.940	0.960	0.985
Source	0.500	0.500	0.500	0.500
Reference	0.900	0.900	0.900	0.900
Sample	0.900	0.900	0.900	0.900
Sample and reference holders	0.900	0.940	0.960	0.985

diffuse. The direction of specular reflection can be computed from the equation

$$\boldsymbol{\omega}_r = \boldsymbol{\omega}_i - 2(\mathbf{n} \cdot \boldsymbol{\omega}_i)\mathbf{n}, \qquad (7)$$

where $\boldsymbol{\omega}_r$, $\boldsymbol{\omega}_i$, and $\mathbf{n}$ are vectors of the direction of reflection, the direction of incidence, and the normal to the surface at the incident point, respectively.

The conventional method[16] for generating random directions in accordance with a Lambertian bidirectional reflectance distribution function involves computation of the coordinates θ and ϕ of the local spherical coordinate system after simple transformation of a pair of pseudorandom numbers according to

$$\theta = \arcsin \sqrt{\eta_\theta}, \qquad \phi = 2\pi\eta_\phi, \qquad (8)$$

with the subsequent transformations to the local Cartesian coordinate system and then to the global system. After global coordinates $(\omega_{rx}, \omega_{ry}, \omega_{rz})$ are determined for the unit vector of the direction of diffuse reflection $\hat{\boldsymbol{\omega}}_r$, the parametric equations of the reflected ray (primed coordinates belong to the initial point of a ray),

$$x = x' + \omega_{rx}t, \qquad y = y' + \omega_{ry}t, \qquad z = z' + \omega_{rz}t, \qquad (9)$$

should be solved together with the equation for each surface inside the IS. The point of next reflection is selected among intercepts of the ray with surfaces as corresponding to the smallest positive value of parameter t. The location of the ray intercept with the spherical surface after diffuse reflection from the same surface can be substantially accelerated by use of the following fact: Every sphere that is tangent to the reflecting surface of a Lambertian reflector in the point of reflection is a surface of uniform irradiance. Therefore, to model the sequence of diffuse reflection points on the internal surface of a sphere it is sufficient to generate the sequence of points uniformly distributed over this surface. We use the algorithm of Marsaglia[17] to obtain the points uniformly distributed on the spherical surface $x^2 + y^2 + z^2 = 1$. The next pair of pseudorandom numbers, η_x and η_y, undergoes the linear transformation

$$u_x = 2\eta_x - 1, \qquad u_y = 2\eta_y - 1. \qquad (10)$$

The points with coordinates $x = u_x$ and $y = u_y$ are uniformly distributed within the square ($-1 < x, y < 1$). If $s = u_x^2 + u_y^2 > 1$, a point is outside the circle of unit radius, the pair of pseudorandom numbers η_x and η_y is rejected, and new pair is generated. Otherwise, the coordinates of the point on the surface of unit sphere are

$$x = 2u_x\sqrt{1-s}, \qquad y = 2u_y\sqrt{1-s}, \qquad z = 1 - 2s. \qquad (11)$$

For a sphere of radius r, the coordinates of the point in Eqs. (9) must be multiplied by the value of r.

After each reflection, the radiance of a ray is multiplied by the value of reflectance at the point of re-
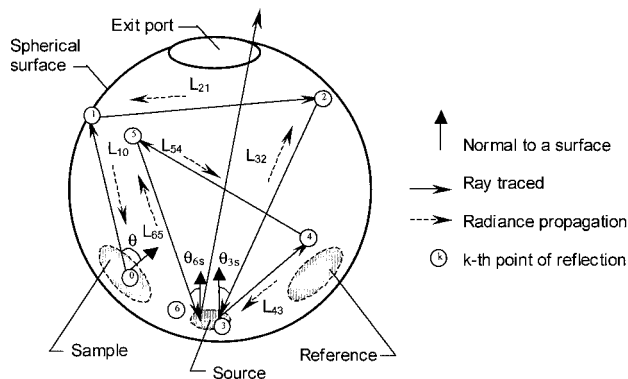
Fig. 4. Schematic of inverse ray tracing.

flection. If the radiance of a ray becomes less than a predefined threshold value (for instance, 0.0001 of the initial value), the trajectory of the ray is terminated. When a ray hits a radiation source, incidence angle θ is calculated. The radiance of a ray, which is considered as emitted by the radiation source, is computed as

$$L_s(\theta) = \frac{\nu + 1}{2\pi} I(0)\cos^{\nu-1}\theta. \qquad (12)$$

A schematic of backward ray tracing is shown in Fig. 4. For simplicity, the baffles are not shown.

In Fig. 4 the ray is traced in the backward direction from point 0 in the center of the sample via points 1, 2, . . . , 6 until it escapes through the exit port. The radiance of this ray propagating from point 6 on the surface of the radiation source via points 5, 4, . . . , 0 is expressed by

$$\begin{aligned} L(\theta) &= \rho_1\rho_2 L_{32} \\ &= \rho_1\rho_2[L_s(\theta_{3s}) + \rho_{3s}\rho_4 L_{54}] \\ &= \rho_1\rho_2[L_s(\theta_{3s}) + \rho_{3s}\rho_4\rho_5 L_{65}] \\ &= \rho_1\rho_2[L_s(\theta_{3s}) + \rho_{3s}\rho_4\rho_5 L_s(\theta_{6s})]. \end{aligned} \qquad (13)$$

Averaging of a large number of trajectories permits evaluation of the radiance of a ray after multiple reflections:

$$L(\theta) = \frac{1}{n}\sum_{i=1}^{n}\sum_{j=1}^{m_i} L_s(\theta_{ij}) \prod_{k=1}^{l_{ij}} \rho_{ijk}, \qquad (14)$$

where n is the number of averaged ray trajectories, m_i is the number of impacts onto the source surface in the ith trajectory, and l_{ij} is the number of reflections between the source and the sample impacts.

To accurately calculate the measured reflectance of the sample, one must compute the radiant fluxes reflected by the sample and reference into the conical solid angles by cosine-weighted averaging over the set of ray trajectories uniformly distributed within the conical solid angle of observation:

$$\rho_{\mathrm{meas}} = \rho_0 \frac{\displaystyle\sum_{i=1}^{n} L_i \cos\theta_i}{\displaystyle\sum_{i=1}^{n} L_{0,i} \cos\theta_{0,i}}, \qquad (15)$$

where L_i and $L_{0,i}$ are the effective (i.e., with multiple reflections taken into account) radiance of the ith ray at the sample and the reference, respectively, and θ_i and $\theta_{0,i}$ are the angles between these rays and normal vectors to the surfaces of the sample and the reference, respectively.

Let us compare the mean number of reflections after which one of two possible events will terminate the trajectory of a ray. If all components of the IS have reflectance ρ and the relative radiance threshold value is γ, the trajectory will be truncated, on average, after

$$n_\gamma = [\log_\rho(\gamma)] = \left\lceil \frac{\ln\gamma}{\ln\rho} \right\rceil \qquad (16)$$

reflections ($[x]$ is the smallest integer greater than or equal to x). For $\rho = 0.98$ and $\gamma = 10^{-4}$, $n_\gamma = 456$.

Assume that all reflections are diffuse. By neglecting the geometrical sizes of baffles, source, sample, and reference, we can evaluate the probability q for a ray to escape through the exit port as the ratio of the port-to-sphere areas. Therefore the mean number of reflections before escape through the exit port could be evaluated as a mathematical expectation:

$$n_p = \sum_{n=1}^{\infty} np_n, \qquad (17)$$

where p_n is the probability for a ray to escape through the exit port after n reflections.

Because $p_n = (1-q)^n q, q < 1$, we can find the sum of the series [Eq. (17)] as[18]

$$n_p = q\sum_{n=1}^{\infty} n(1-q)^n = \frac{1-q}{q}. \qquad (18)$$

If the half-axes of the elliptical port are $r_{0x} = 30$ mm and $r_{0y} = 23$ mm, and the sphere radius is 127 mm, then q is ~0.01 and $n_p = 0.99$. By neglecting the geometrical sizes of baffles, exit port, sample, and reference, we can evaluate the mean number of reflections $n_s = (1-r')/r'$ before the first ray–source intersection (r' is the source-to-sphere area ratio). For $r' = 0.0004$, n_s is ~2500. The interrelation among n_γ, n_p, and n_s reveals that only a few of the trajectories carry at least one point that belongs to the source; many of the rays were traced with no contribution to the computed radiance. This is the reason for the slow convergence of the brute force algorithm that we have described.
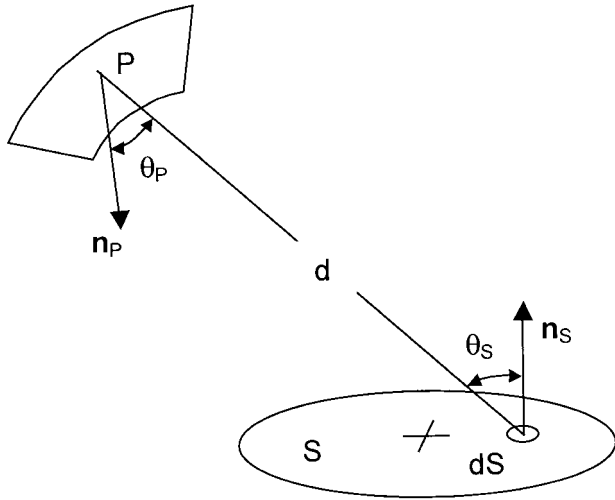
Fig. 5. Schematic for calculation of irradiance produced by source S at point P.

Fig. 6. Schematic of the shadow rays algorithm.

5. Shadow Rays Algorithm

To perform the parametric studies for our model of the IS it was necessary to implement a new algorithm to accelerate the unacceptably slow convergence of the computational process. (Computation of the hemispherical distribution of radiance incident onto a sample on the grid of 91×181 nodes with a random uncertainty of 0.1% requires as many as 90 h on a 2.2-GHz Pentium IV processor PC. Note that the grid of 91×181 nodes is too coarse for the small-scale features of radiance maps to be detected). The key element of the improved algorithm is the use of an analytical computation of irradiance produced by the direct source radiation for each point of diffuse reflection. The irradiation on point P of any surface (see Fig. 5) is equal to

$$E(P) = \int_S V(P, \mathrm{d}S) L_s(\theta_S) \frac{\cos \theta_S \cos \theta_P}{\pi d^2} \mathrm{d}S, \quad (19)$$

where S is the area of a source; V is a vignetting function, which is equal to 1 if no obstruction exist between point P and the element $\mathrm{d}S$ of a source and is equal to 0 otherwise; θ_S and θ_P are angles between normals $\mathbf{n}_P$ and $\mathbf{n}_S$, respectively, and the straight line of length d connecting point P and element $\mathrm{d}S$.

In a discrete form suitable to Monte Carlo ray-tracing techniques, Eq. (19) can be rewritten as

$$E_i = \frac{S}{m} \sum_{j=1}^{m} V_{ij} L_S(\theta_j) \frac{\cos \theta_i \cos \theta_j}{\pi d_{ij}^2}, \quad (20)$$

where m is the number of random points chosen on the surface of a source. An analogous technique in computer graphics is called the shadow rays algorithm.[19]

The calculations by Eq. (20) are time consuming, and the time of computation grows proportionally to m. The numerical experiments performed shown that $m = 1$ is the optimal value by the criterion of
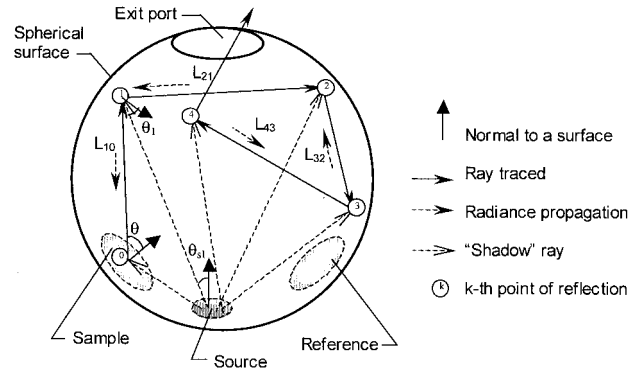
maximum accuracy for the fixed time of computation. Algorithmically this means that we shall generate only one random point on the source surface for each diffuse reflection of ray traced (see Fig. 6). Some loss of accuracy in the radiance of a single ray is compensated for by an increase in the number of rays traced.

If 1, 2, 3, ... is a series of intercepts obtained as a result of the application of the directional importance sampling method to the IS with all Lambertian surfaces, then (Fig. 6)

$$L_{i,0}(\theta) = L_{s0}(\theta_0) V_{s0} + \rho_1 \left(\frac{1}{\pi} E_1 + \rho_2 \left\{ \frac{1}{\pi} E_2 + \rho_3 \left[\frac{1}{\pi} E_3 \right. \right. \right.$$
$$\left. \left. \left. + \rho_4 \left(\frac{1}{\pi} E_4 + \dots \right) \right] \right\} \right)$$
$$= L_{s0}(\theta_0) V_{s0} + \frac{1}{\pi} (\rho_1 E_1 + \rho_1 \rho_2 E_2 + \rho_1 \rho_2 \rho_3 E_3$$
$$+ \rho_1 \rho_2 \rho_3 \rho_4 E_4 + \dots)$$
$$= L_{s0}(\theta_0) V_{s0} + \frac{1}{\pi} \sum_{j=1}^{m} E_j \prod_{k=1}^{l_j} \rho_k \quad (21)$$

Taking into account that

$$E_j = S V_{ss_j} L_s(\theta_{s_j}) \frac{\cos \theta_{s_j} \cos \theta_j}{\pi d_{s_j,j}^2}, \quad (22)$$

we can obtain

$$L_0(\theta) = \frac{1}{n} \sum_{i=1}^{n} \left[L_{S_i 0}(\theta_0) V_{S_i 0} + \frac{S}{\pi^2} \sum_{j=1}^{m_i} L_S(\theta_{S_{ij}}) \right.$$
$$\left. \times \frac{\cos \theta_{S_{ij}} \cos \theta_{ij}}{d_{S_{ij}}^2} V_{S_{ij}} \prod_{k=1}^{l_{ij}} \rho^k \right]. \quad (23)$$

The flow chart for this algorithm is depicted in Fig. 7.

The substantial reduction in total computation time has been achieved by the use of a time-saving recipe known by various names: method of dependent trials (tests),[20] method of correlated sampling,[21] etc. In essence, in our case we utilize the same set of ray trajectories for evaluation of the IS reflectometer with different reflectances but the same specularity values for its surfaces. According to this method, we assign a set of M statistical weights to each ray and
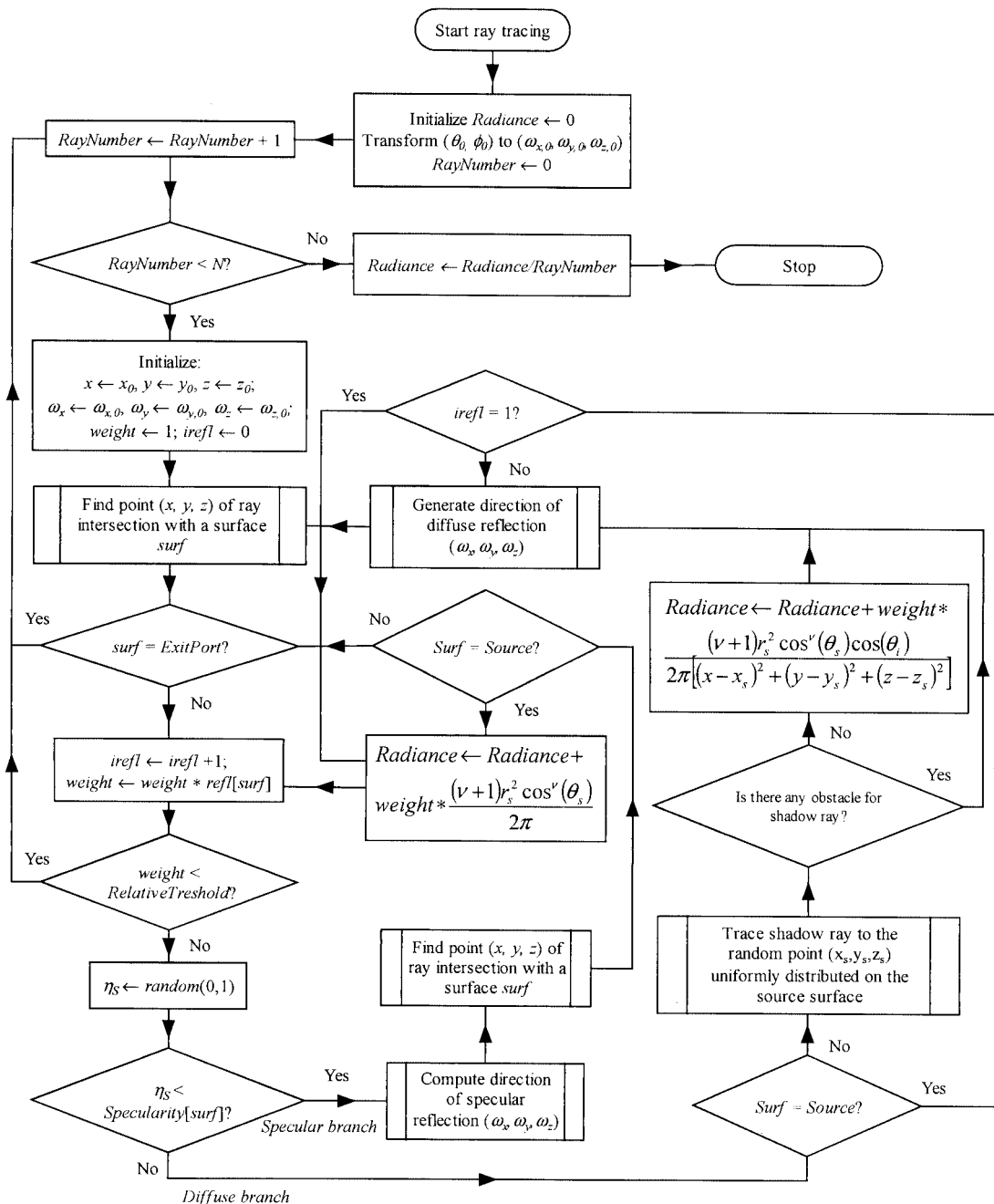
Fig. 7. Flow chart of the algorithm for computing radiance.

a corresponding set of M reflectance values to every surface. After each reflection, the statistical weights are transformed as

$$w_{r,i} = \rho_i w_i, \qquad i = 1, 2, \ldots, M, \qquad (24)$$

where ρ_i is the reflectance of a surface and w_i and $w_{r,i}$ are the statistical weights of a ray before and after reflection, respectively.

The bilateral symmetry of the IS about the image plane enables one to reduce the random uncertainty of the computed distributions of radiance incident onto the sample's center by averaging the radiances that come from symmetrical directions. However,

these distributions are intended primarily for visual perception and evaluation of the IS quality. Therefore we prefer to not use this implicit approach because it leads to formation of symmetrical patterns on the radiance maps.

6. Notes on the Performance of Pseudorandom-Number Generators

A distinctive feature of these modeling studies is the necessity to perform large series of Monte Carlo trials. For example, for the computation of the radiance angular distribution for radiation incident onto the center of the sample or reference, $181 \times 361 =$
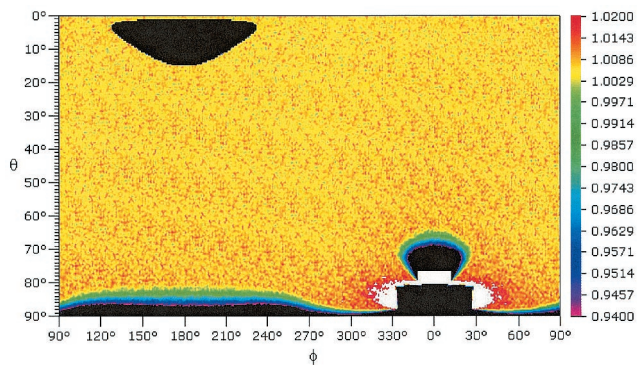
Fig. 8. Artifactual pattern in a color map of the hemispherical distribution of radiance incident onto a sample center (a standard commercial PRNG was used).

65341 nodes of the hemispherical mesh were used. For every direction we employed as many as 100,000 rays; each trajectory contains as many as 100 consecutive reflections. When all reflections are diffuse, we must have on average approximately three pseudorandom numbers for each direction. Obviously, the period of the pseudo-random number generator (PRNG) must be greater than the total expenditure of random numbers, i.e., more than 2×10^{12}. Another requirement for the PRNG is good equidistribution.[22] The property of t equidistribution means that the PRNG must generate such pseudorandom numbers that the t-dimensional points formed by subsequences of pseudorandom numbers of length t should be uniformly distributed over the t-dimensional unit hypercube. The majority of commercially available PRNGs have poor equidistribution.[23] In our case, the use of such a PRNG with a measured period of $4,294,967,296 = 2^{32}$ in the first version of the program resulted in the appearance of artifactual periodic patterns of inclined stripes in the radiance distributions (see Fig. 8). All artifacts disappeared (see Fig. 9) after replacement of this PRNG with the so-called Mersenne Twister generator,[24] which provides an extremely large period of $2^{19937} - 1$ and 623-dimensional equidistribution up to 32-bit accuracy.
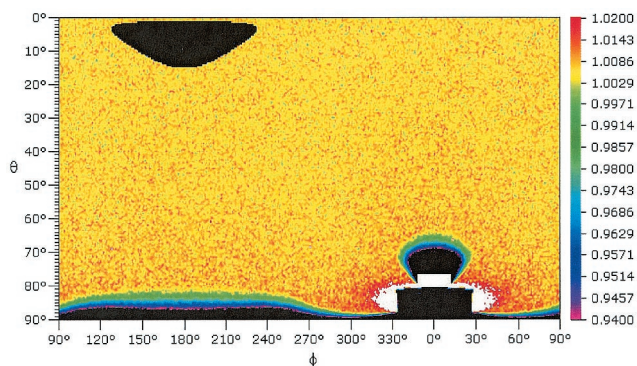
Currently, the Mersenne Twister generator is

Fig. 9. Same distribution as in Fig. 8 but computed with the use of a Mersenne–Twister PRNG.

freely distributed software. The codes for its algorithm in various programming languages can be found on the Web at http://www.math.keio.ac.jp/~matumoto/emt.html.

7. Results of Numerical Experiments

At the initial stage of modeling, the convergence of the computational process was investigated. It was determined that not fewer than 10^7 rays are required for achievement of a standard deviation of computed radiance of $\sim 0.1\%$ when the brute force method is used but only $\sim 10^5$ rays are needed when the shadow rays algorithm is used. Even though the time required for modeling a single trajectory by the shadow rays algorithm is several times greater than that for the brute force algorithm, overall the shadow rays algorithm is significantly faster. Depending on the input data used, we obtained a 5- to 15-fold advantage with the use of the shadow rays algorithm. This is true for ISs with all diffuse surfaces. As the specularity of the sphere surface increases, the efficiency of the shadow rays algorithm decreases, eventually approaching that of the brute force algorithm.

To evaluate the performance of the sphere, we examined the effects of important parameters on a sample's measured reflectance. To develop an understanding of why and how these effects occur we examined the radiance distributions. All aspects of algorithm performance are equally true for both of these ways of examining sphere performance. The computed hemispherical distributions of radiance falling upon the sample center were normalized by division by their weighted mean values:

$$\bar{L} = \frac{\sum_{i=1}^{N_\theta} \sin \theta_i \sum_{j=1}^{N_\phi} L_{ij}}{n_j \sum_{i=1}^{N_\theta} \sin 2\theta_i}, \qquad (25)$$

where weighting factors $\sin 2\theta_i$ are proportional to projected solid angles of appropriate cells of the hemispherical mesh. Cylindrical projections of these distributions are shown in the color figures (Figs. 10–17). Black color indicates that the radiance is less than the lower limit of the color scale at the right in each figure; white indicates a level above the upper limit. For purposes of comparison, the relative radiance range 0.9–1.1 is the same for all those figures. The black area with its center at $\theta = 7°$, $\phi = 180°$ is the projection of the elliptic exit port (zero radiance). The dark quadrangle lying on the bottom axis close to $\phi = 0°$ is the projection of the baffle between the radiation source and the sample.

Figures 10–13 present these distributions for an IS reflectometer composed only of purely diffuse surfaces and for a Lambertian radiation source. Each of these figures corresponds to one variant of the surfaces reflectances from Table 2. The sequence of Figs. 10–13 illustrates the improvement in the radiance distribution nonuniformity from 10–12% to 2–3% as the sphere reflectance increases from 0.9 to 0.99. As a result of the use of the method of corre-
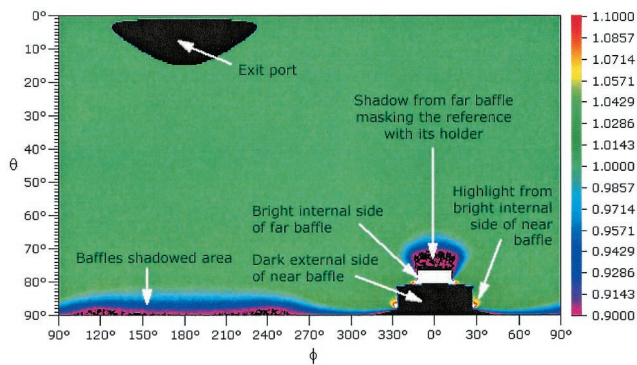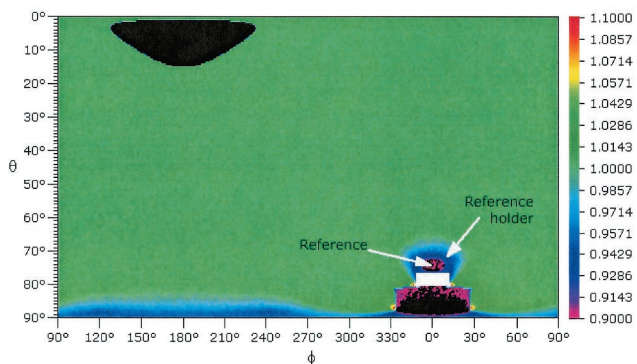
Fig. 10.   Hemispherical distribution of radiance incident onto the sample center; 10,000 rays were traced for every $N_\theta \times N_\phi = 181 \times 361$ points of a uniform grid.   Radiation source with $\nu = 1$.   All specularities are 0; reflectances from Variant 1 of Table 2.
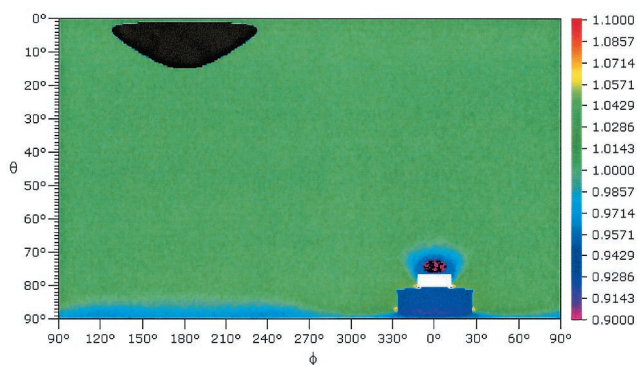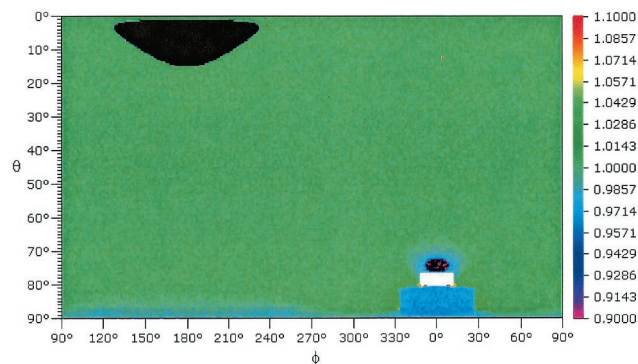

Fig. 13.   Hemispherical distribution of radiance incident onto the sample center; 10,000 rays have been traced for every $N_\theta \times N_\phi = 181 \times 361$ points of a uniform grid.   Radiation source with $\nu = 1$. All specularities are 0; reflectances from Variant 4 of Table 2.

lated sampling, we obtained the output values for all four values of sphere reflectance in Table 2 from a single run of the program.

In Figs. 10, 14, and 15 the radiant intensity distribution $I(\theta)$ of the radiation source [see Eq. (6) and Fig. 3] is varied, with $\nu = 1, 0.5, 2$, respectively.   For

those figures all surfaces are purely diffuse and the wall reflectance is 0.90 (Variant 1, Table 2).   A comparison of these figures illustrates the importance of the initial first-bounce irradiance distribution of the sphere on the nonuniformity of the sample's incident radiance distribution.   Even for a wall reflectance of

Fig. 11.   Hemispherical distribution of radiance incident onto the sample center; 10,000 rays were traced for every of $N_\theta \times N_\phi = 181 \times 361$ points of a uniform grid.   Radiation source with $\nu = 1$. All specularities are 0; reflectances from Variant 2 of Table 2.
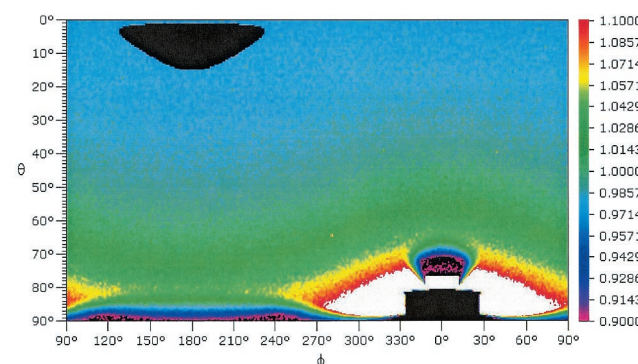

Fig. 14.   Hemispherical distribution of radiance incident onto the sample center; 10,000 rays have been traced for every $N_\theta \times N_\phi = 181 \times 361$ points of a uniform grid.   Radiation source with $\nu = 0.5$. All specularities are 0; reflectances from Variant 1 of Table 2.

Fig. 12.   Hemispherical distribution of radiance incident onto the sample center; 10,000 rays have been traced for every of $N_\theta \times N_\phi = 181 \times 361$ points of a uniform grid.   Radiation source with $\nu = 1$. All specularities are 0; reflectances from Variant 3 of Table 2.
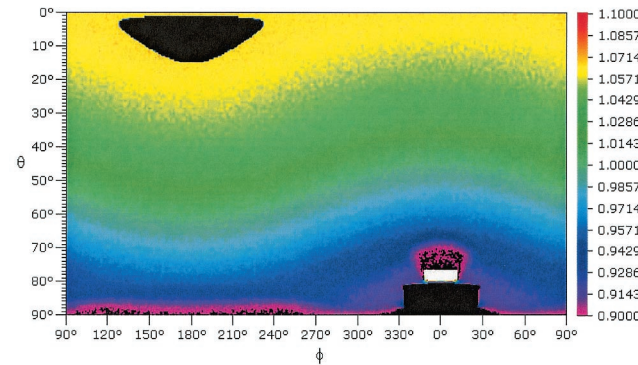

Fig. 15.   Hemispherical distribution of radiance incident onto the sample center; 10,000 rays have been traced for every $N_\theta \times N_\phi = 181 \times 361$ points of a uniform grid.   Radiation source with $\nu = 2$. All specularities are 0; reflectances from Variant 1 of Table 2.
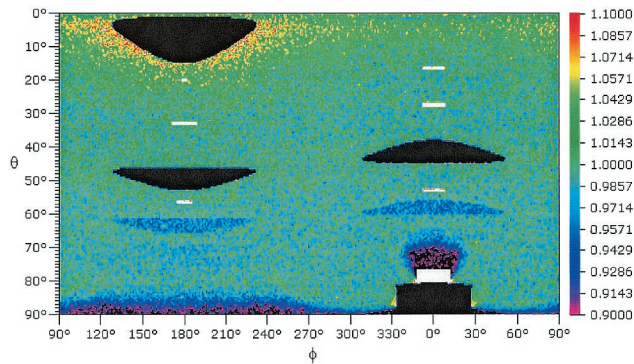
Fig. 16. Hemispherical distribution of radiance incident onto the sample center; 50,000 rays have been traced for every $N_\theta \times N_\phi = 181 \times 361$ points of a uniform grid. Radiation source with $\nu = 1$. Sphere and baffles specularities are 0.2; all other specularities are 0; reflectances from Variant 1 of Table 2.

Fig. 18. Measured sample reflectance relative to sphere and baffle specularity for several values of sample specularity. Reference specularity is 0; reflectances from Variant 1 of Table 2; $\nu = 1$. Sample specularity: ●, 0; ○, 0.2; ◆, 0.4; ◇, 0.6; ▼, 0.8; and ▽, 1.

0.97 (not shown) one finds variations of 8–10% in the radiance distribution for both $\nu = 0.5$ and $\nu = 2$.

The effects of adding a specular component to the reflection of the IS internal surface are shown in Figs. 16 and 17, which illustrate the abrupt transformation in the distribution of incident radiance. In these distributions we can observe the series of erect and inverted images of the radiation source and the opening, with the decreasing intensities. In reality, the reflectance from specular-diffuse surfaces contains a specular lobe rather than a specular spike; thus the sharp edges of the images that one can observe in Figs. 16 and 17, especially the higher orders, will be significantly reduced. Nevertheless, any deviation from a perfectly diffuse surface can be expected to result in nonuniformity of the radiance distributions, and the results from the specular-diffuse case can be expected to describe qualitatively the results from a more-realistic lobed specular configuration.

These radiance distributions and additional studies can be used for visual analysis of the sphere reflectometer and to perform design optimization. Our numerical model of the IS reflectometer will also be

useful in the mathematical processing of experimental data. For a comparison of a specular-diffuse sample with a diffuse reference, a systematic uncertainty may occur. Its value should be a complicated function of system geometry, optical characteristics of the surfaces included in the system under modeling, etc.

In Fig. 18 the dependence of the measured sample reflectance on sphere and baffle specularity is shown for six values of sample specularity. Reflectance values have been taken from Variant 1 of Table 2. The largest uncertainties occur for high specularities of the sample and internal surface of the IS. The uncertainty remains small for sphere and baffle specularity less than 0.5. This region is expanded in the inset of Fig. 18.

A comparison of a purely specular sample with a purely diffuse reference is the extreme case for systematic uncertainty in such a measurement. In Fig.
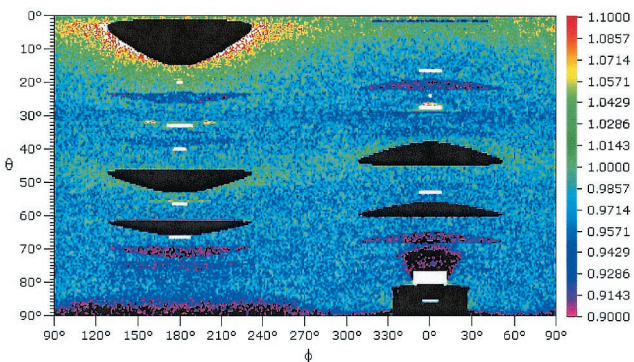

Fig. 17. Hemispherical distribution of radiance incident onto the sample center; 80,000 rays have been traced for every $N_\theta \times N_\phi = 181 \times 361$ points of a uniform grid. Radiation source with $\nu = 1$. Sphere and baffles specularities are 0.4; all other specularities are 0; reflectances from Variant 1 of Table 2.
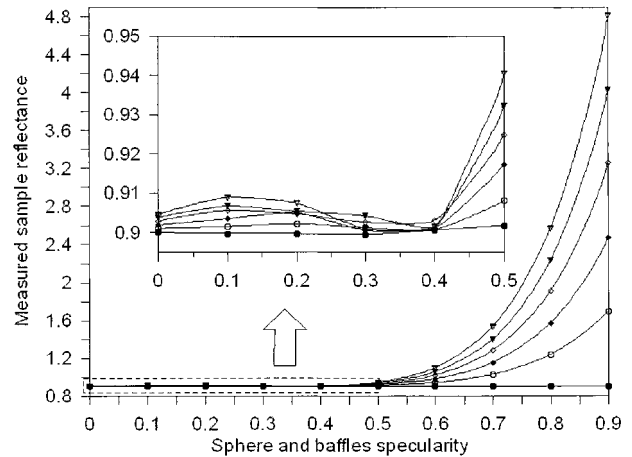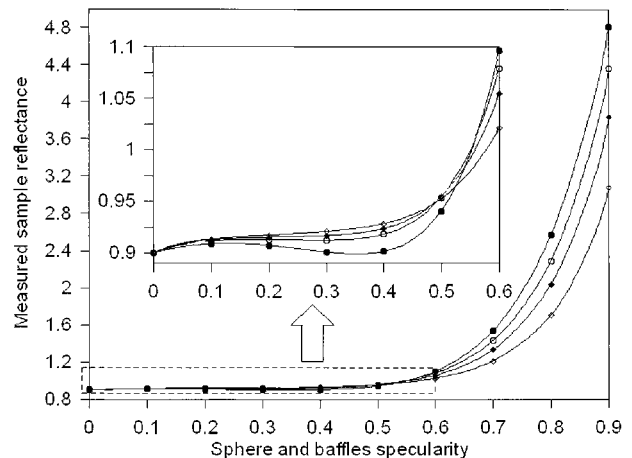

Fig. 19. Measured reflectance of a purely specular sample relative to sphere and baffle specularity. Reference specularity is 0; $\nu = 1$. For four variants of reflectance from Table 2. Variant: ●, 1; ○, 2; ◆, 3; and ◇, 4.

19 the dependence of the measured reflectance of a purely specular sample on sphere and baffle specularity is depicted for four variants of surface reflectance values from Table 2. For high values of sphere and baffle specularity, the maximum deviation from the true value is obtained for ISs with low values of internal surface reflectance. But for sphere and baffle specularity less than 0.5 (Fig. 19, inset), we can observe an inversion of this order.

To achieve a level of random uncertainty of the computation of less than 0.1% (in the majority of cases, of less than 0.05%), we used 10 trials, with 10^7 rays in each. Calculations of the mean value and standard deviation were used for every point shown in Figs. 18 and 19.

8. Conclusion and Prospects for Further Development

We have developed a flexible algorithm and specialized software intended for efficient numerical modeling of an integrating sphere reflectometer. The resultant program was applied to modeling of a specific measurement facility. We used the program to compute the hemispherical distributions of radiance for radiation incident onto a sample in the reflectometer. The influence of critical factors such as the angular distribution of radiant intensity of the radiation source and the reflectance and specularity of the sphere's internal surface was examined. Corrections for the systematic uncertainty that is due to specular components of reflection of the sample and the IS internal surface were computed.

We shall use the radiance distributions shown in this paper to obtain uncertainty contributions to the eventual measurements of sample reflectance. No analytical methods for performing this type of analysis are available. The results will also be used to improve the eventual sphere design. Some obvious routes to improvement include adjusting the baffle reflectances on both sides to better match the surrounding radiance levels and making a significant effort to produce as nearly as possible a Lambertian distribution for the input light source. (The analogous requirement to be met for a directional-hemispherical design would be to have a detector with uniform response relative to input angle.)

Although we used distribution of radiation source radiant intensity proportional to $\cos^\nu \theta$, the software permits incorporation of an arbitrary distribution, including a measured distribution, with interpolation between tabulated values. We plan also to incorporate into our reflectometer model program the procedure for sampling of the directions of reflection in accordance with physically plausible bidirectional reflectance distribution functions for all sphere components.

We have developed a fast and reliable ray-tracing algorithm that can be used for numerical modeling of various IS-based instruments, including measurement of the optical characteristics of opaque and transparent materials, and for production of an extended uniform-radiance calibration source.[25]

References

1. D. G. Goebel, "Generalized integrating-sphere theory," Appl. Opt. **6,** 125–128 (1967).
2. M. W. Finkel, "Integrating sphere theory," Opt. Commun. **2,** 25–28 (1970).
3. W. B. Fussell, "Approximate theory of the photometric integrating sphere," Natl. Bur. Stand. (U.S.) Tech. Note **594-7** (1974).
4. R. L. Brown, "A numerical solution of the integral equation describing a photometric integrating sphere," J. Res. Natl. Bur. Stand. Sect. A **77,** 343–351 (1973).
5. A. C. M. De Visser and M. Van der Woude, "Minimization of the screen effect in the integrating sphere by variation of the reflection factor," Light. Res. Technol. **12,** 42–49 (1980).
6. Y. Ohno, "Integrating sphere simulation: application to total flux scale realization," Appl. Opt. **33,** 2637–2646 (1994).
7. H. L. Tardy, "Matrix method for integrating sphere calculations," J. Opt. Soc. Am. A **8,** 1411–1418 (1991).
8. J. F. Clare, "Comparison of four analytic methods for the calculation of irradiance in integrating spheres," J. Opt. Soc. Am. A **15,** 3086–3096 (1998).
9. L. M. Hanssen, "Effects of non-Lambertian surfaces on integrating sphere measurements," Appl. Opt. **35,** 3597–3606 (1996).
10. A. V. Prokhorov, V. I. Sapritsky, and S. N. Mekhontsev, "Modeling of integrating spheres for photometric and radiometric applications," in *Optical Radiation Measurements III*, J. M. Palmer, ed., Proc. SPIE **2815,** 118–125 (1996).
11. B. G. Crowther, "Computer modeling of integrating spheres," Appl. Opt. **35,** 5880–5886 (1996).
12. A. Ziegler, H. Hess, and H. Schimpl, "Rechnersimulation von Ulbrichtkugeln," Optik (Stuttgart) **101,** 130–136 (1996).
13. F. E. Nicodemus, J. C. Richmond, J. J. Hsia, I. W. Ginsberg, and T. Limperis, "Geometrical considerations and Nomenclature for Reflectance," Natl. Bur. Stand. (U.S.) Monogr. **160,** 11–12 (1977).
14. P. Shirley, C. Wang, and K. Zimmerman, "Monte Carlo techniques for direct lighting calculations," ACM Trans. Graphics **15,** 1–36 (1966).
15. P. Shirley, *Realistic Ray Tracing*, (A K Peters, Natick, Mass., 2000).
16. R. Siegel and J. R. Howell, *Thermal Radiation Heat Transfer*, 3rd ed. (Taylor & Francis, Washington, D.C., 1992).
17. G. Marsaglia, "Choosing a point from the surface of a sphere," Ann. Math. Stat. **43,** 645–646 (1972).
18. I. S. Gradshteyn and I. M. Ryzhik, *Table of Integrals, Series, and Products*, 6th ed. (Academic, San Diego, Calif., 2000).
19. E. Lafortune and Y. Willems, "A theoretical framework for physically based rendering," Comput. Graph. Forum **13,** 97–107 (1994).
20. I. Manno, *Introduction to the Monte-Carlo Method* (Akademiai Kiado, Budapest, 1999).
21. J. Spanier and E. M. Gelbard, *Monte Carlo Principles and Neutron Transport Problems* (Addison-Wesley, Reading, Mass., 1969).
22. P. L'Ecuyer, "Uniform random number generators," in *Proceedings of 1998 Winter Simulation Conference* (Association of Computing Machinery, New York, 1998), p. 104.
23. K. Entacher, "Bad subsequences of well-known linear congruential pseudorandom number generators," ACM Trans. Modeling Comput. Simulation **8,** 61–70 (1998).
24. M. Matsumoto and T. Nishimura, "Mersenne Twister: a 623-dimensionally equidistributed uniform pseudo-random number generator," ACM Trans. Modeling Comput. Simulation **8,** 3–30 (1998).
25. A. V. Prokhorov and L. M. Hanssen, "Numerical modeling of an integrating sphere radiation source," in *Modeling and Characterization of Light Sources*, C. B. Wooley, ed., Proc. SPIE **4775,** 106–118 (2002).